Nano-TiNb$_2$O$_7$/carbon nanotubes composite anode for enhanced lithium-ion storage

CrossMark

Chunfu Lin [a], Lei Hu [a], Chuanbing Cheng [b], Kai Sun [b], Xingkui Guo [c], Qian Shao [c], Jianbao Li [a], Ning Wang [a, **], Zhanhu Guo [b, *]

[a] State Key Laboratory of Marine Resource Utilization in South China Sea, College of Materials and Chemical Engineering, Hainan University, Haikou 570228, PR China
[b] Integrated Composites Laboratory (ICL), Department of Chemical and Biomolecular Engineering, University of Tennessee, Knoxville, TN 37996, USA
[c] College of Chemical and Environmental Engineering, Shandong University of Science and Technology, Qingdao 266590, PR China

ARTICLE INFO

ABSTRACT

Although with a large capacity, TiNb$_2$O$_7$ as an anode material of lithium-ion batteries suffers from a poor rate capability. To solve this challenge, nano-TiNb$_2$O$_7$ and its carbon nanotube (CNT) nanocomposites were prepared by direct hydrolysis of TiNb$_2$O$_7$/CNTs suspension followed by calcination in air and N$_2$, respectively. The TiNb$_2$O$_7$ nanoparticles in the composites have a Ti$_2$Nb$_{10}$O$_{29}$-type crystal structure with O^{2-} vacancies and lower-valence cations, leading to improved Li$^+$-ion diffusion coefficient and increased electronic conductivity in TiNb$_2$O$_7$. The evenly distributed CNTs have good contact with the TiNb$_2$O$_7$ particles, thereby reducing their particle sizes and improving the electrical conduction. As a result of these improvements, the nanocomposites present outstanding electrochemical performances. For example, it delivers a large reversible capacity (346 mAh g^{-1} at 0.1 C) and a prominent rate capability (still 163 mAh g^{-1} at the ultra-large current rate of 30 C). Exceptional cyclic stability is also demonstrated with over 100 cycles at 10 C with large capacity retention of 97.6%. These results reveal that the nano-TiNb$_2$O$_7$/CNTs composites can be a promising anode material for lithium-ion batteries of electric vehicles.

© 2017 Elsevier Ltd. All rights reserved.

1. Introduction

Lithium-ion batteries (LIBs) have been used as salient energy storage devices for portable electronics in the past two decades. This great success is now being extended to electric vehicles (EVs) [1]. In this regard, high energy density, power density, safety and cyclic stability are required for the LIBs of EVs. However, current commercial LIBs with lithiated transitional-metal oxide cathodes and graphite anodes cannot fulfill these requirements. Especially, although the graphite anode has a large capacity, low cost and good cyclic stability, it suffers from several severe issues [2–4]. For instance, its low working potential of ~0.1 V *vs.* Li/Li$^+$ causes the generation of passivating solid-electrolyte interphase (SEI) layers, which results in irreversible lithium loss and insufficient electrochemical kinetics. Moreover, lithium dendrites could be formed and continuously grow to penetrate the separator and contact the

two electrodes, bringing about short circuit or burning the flammable electrolyte. To overcome these drawbacks, it is highly desirable to explore alternative anode materials which can fulfill the above four requirements.

Spinel Li$_4$Ti$_5$O$_{12}$ has been intensively investigated due to its relatively high working potential of ~1.55 V [5]. Such high working potential avoids the formation of SEI layers and lithium dendrites. After modified, it can have good safety, rate capability and cyclic stability. However, its theoretical capacity is rather small (175 mAh g^{-1}) on the basis of only three transferred electrons/Li$^+$-ions per Li$_4$Ti$_5$O$_{12}$ formula unit in 3.0–1.0 V, which results in very low energy density. To tackle this issue, TiNb$_2$O$_7$ is of more interest due to its large specific capacity [6]. It shows a monoclinic shear ReO$_3$ crystal structure with *C*2/*m* space group (Fig. 1a), which is built by 3 × 3 × ∞ ReO$_3$-type octahedral-blocks sharing edges and corners. The containing redox couples of Ti^{3+}/Ti^{4+}, Nb^{4+}/Nb^{5+} and Nb^{3+}/Nb^{4+} lead to its enormously large theoretical capacity of 388 mAh g^{-1}, which is 122% larger than that of Li$_4$Ti$_5$O$_{12}$ (175 mAh g^{-1}) and even surpasses that of graphite (372 mAh g^{-1}). Similar to Li$_4$Ti$_5$O$_{12}$, TiNb$_2$O$_7$ shows a relatively high working

---

* Corresponding author.
** Corresponding author.
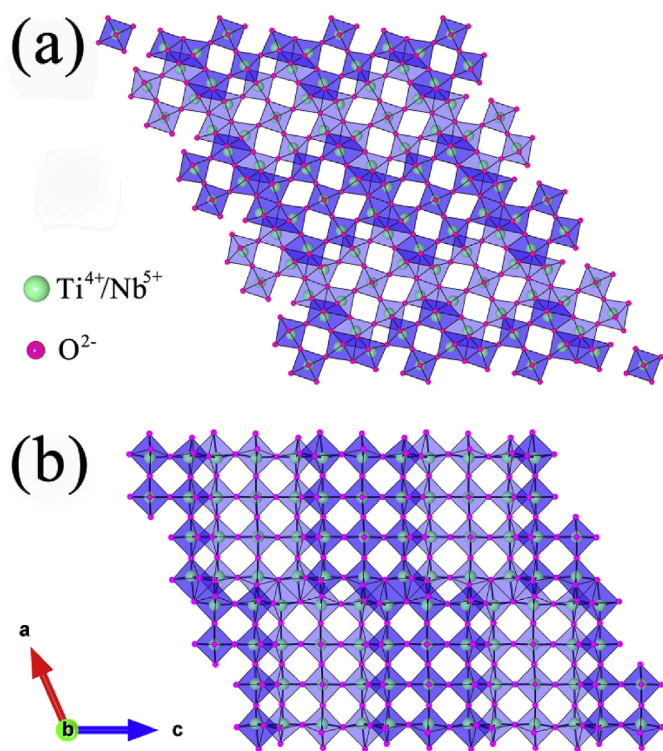*E-mail addresses:* wangn02@foxmail.com (N. Wang), zguo10@utk.edu (Z. Guo).

Fig. 1. Crystal structures of (a) $TiNb_2O_7$ and (b) $Ti_2Nb_{10}O_{29}$.

potential (~1.6 V), avoiding the issues of SEI layers and lithium dendrites. Despite of large capacity and good safety, $TiNb_2O_7$ suffers from its intrinsically poor conductivity. The valences of Ti and Nb elements in $TiNb_2O_7$ are +4 and + 5, respectively. The empty $3d/4d$ orbitals in the Ti^{4+}/Nb^{5+} ions indicate that no free electrons can participate in the electronic conduction, leading to its insulator characteristic and extremely small electronic conductivity ($<10^{-9}$ S cm^{-1}) [7]. Meanwhile, its Li^+-ion diffusion coefficient is rather limited [8]. Consequently, its rate capability is low. The reported methods to increase the rate capability of $TiNb_2O_7$ include modifying crystal structure, compositing conductive phases, and reducing particle sizes [8–27]. A combined method is generally more effective to improve the rate capability than separate methods [28,29]. For instance, Lin and co-workers employed a method combining Cr^{3+} substitution, carbon nanotube (CNT) compositing and particle-size reduction to greatly improve the rate capability of $Li_4Ti_5O_{12}$ [28]. The resultant nanosized $LiCrTiO_4$/CNTs composite exhibited an excellent rate capability with a large capacity of 120 mAh g^{-1} at 10 C, while those for microsized $LiCrTiO_4$/CNTs, microsized $LiCrTiO_4$ and microsized $Li_4Ti_5O_{12}$ were 106, 70 and 11 mAh g^{-1}, respectively. They also prepared mesoporous $Li_4Ti_5O_{12-x}$/C submicrospheres containing Ti^{3+} ions, O^{2-} vacancies, carbon particles/coatings, and nanosized primary particles/pores [29], which showed an outstanding rate capability. At 10 C, the optimized sample delivered a large capacity of 119 mAh g^{-1}.

In this study, for the first time, a method combining crystal structure modification, CNT compositing and nanosizing is adopted to improve the electrochemical performances of $TiNb_2O_7$. A novel nanosized $TiNb_2O_7$/CNTs composite (nano-$TiNb_2O_7$/CNTs) is synthesized through direct hydrolysis of $TiNb_2O_7$/CNTs suspension followed by calcination in N_2. For comparison, pure nanosized $TiNb_2O_7$ particles (nano-$TiNb_2O_7$) are synthesized through the same method but calcined in air. This combined method effectively enhances the electronic conductivity and Li^+-ion diffusion

coefficient in the $TiNb_2O_7$ particles, reduces the $TiNb_2O_7$ particle sizes and improves the electrical conduction among the adjacent $TiNb_2O_7$ particles. Consequently, this composite exhibits advantageous electrochemical performances in term of large specific capacity (346 mAh g^{-1} at 0.1 C), safe working potential (~1.6 V), high rate capability (163 mAh g^{-1} at 30 C) and good cyclic stability (capacity retention of 97.6% after 100 cycles), thereby fulfilling the four requirements of the LIBs in EVs.

2. Experimental

2.1. Materials preparations

0.01 mol titanium isopropoxide ($Ti(OC_3H_7)_4$, Sigma–Aldrich, 97%) was added into 40 mL ethanol in a beaker with proper stirring. Then, 0.02 mol niobium chloride ($NbCl_5$, Aladdin, 99.9%) was added into the above solution with vigorous stirring at 40 °C until a light suspension was formed. The CNTs with an average diameter of 40–60 nm (Shenzhen Nanotech Port Co. Ltd.) were added into a 6 M HNO_3 solution, nitrified for 0.5 h, vacuum filtrated, washed by deionized water, and vacuum dried at 80 °C, producing functional groups on the CNT surface [30–32]. The pretreated CNTs and $TiNb_2O_7$ suspension with a weight ratio of 1:10 were mixed and stirred at 60 °C until the solvent was completely volatilized. The functional groups would help the nucleation of deposits through certain interactions with metal ions [30–32]. The resultant powders were calcined at 700 °C for 2 h in a N_2 atmosphere to obtain the well crystallized nano-$TiNb_2O_7$/CNTs composite. For comparison, pure nano-$TiNb_2O_7$ was synthesized with the similar manner except for calcination in an air atmosphere.

2.2. Materials characterizations

The crystal structures of the as-calcined powders were characterized by powder X-ray diffraction (XRD) using an X-ray diffractometer (Bruker D8 Advance, Germany, Cu-K_α radiation source $\lambda = 1.5406$ Å). The morphologies (particle sizes and microstructures) were investigated using a field emission scanning electron microscopy (FESEM, Hitachi S-4800, Japan) and a high-resolution transmission electron microscopy (HRTEM, FEI Tecnai G2 F20 S-TWIN, USA). Brunauer–Emmett–Teller (BET) specific surface areas and Barrett–Joyner–Halenda (BJH) pore size distributions were obtained from standard N_2 adsorption–desorption isotherms measured by a surface area analyzer (ASAP 2020, USA).

2.3. Electrochemical tests

Electrochemical performances were evaluated using CR2016-type coin cells, which were assembled in a dry argon-filled glove box. 65 wt% as-calcined powders, 10 wt% polyvinylidene fluoride (PVDF) and 25 wt% conductive carbon (Super P®) were thoroughly mixed in N-methylpyrrolidone (NMP), forming a homogeneous slurry. The slurry was uniformly cast onto Cu foils, which were then vacuum-dried at 120 °C for 10 h and finally roller-pressed by a rolling machine to form the working electrodes. The mass loading of the active materials was ~1.4 mg cm^{-2}. Li foils acted as counter and reference electrodes. Microporous polypropylene films (Celgard 2325) were employed as separators. A 1 M solution of $LiPF_6$ (DAN VEC) in ethylene carbonate (EC)/dimethyl carbonate (DMC)/diethylene carbonate (DEC) with a volume ratio of 1: 1: 1 was used as electrolyte. Galvanostatic discharge–charge tests were performed at various current rates using a multi-channel battery testing system (Neware CT-3008, China) in a potential range of 3.0–0.8 V. Cyclic voltammetry (CV) and electrochemical impedance spectroscopy (EIS) measurements were carried out using an

electrochemical workstation (Zahner Zennium, Kronach, Germany). The set CV scan speeds were in a range of 0.2–1.1 mV s^{-1}. The impedance spectra were recorded in a frequency range of 10^5–10^{-2} Hz. Before the EIS measurements, the cells were discharged to 50% state of charge, followed by two discharge–charge cycles and then equilibrated for 5 h.

3. Results and discussion

3.1. Material characteristics

Fig. 2 displays the XRD patterns of nano-$TiNb_2O_7$ and its CNT nanocomposite. As can be seen, all the XRD peaks of nano-$TiNb_2O_7$ match well with those of monoclinic $TiNb_2O_7$ with $C2/m$ space group (JCPDS card No. 77-159). No impurity phases can be found. This result together with the white color of nano-$TiNb_2O_7$ suggests that nano-$TiNb_2O_7$ is pure and that the crystal growth of the monoclinic $TiNb_2O_7$ structure is not destroyed by the addition of CNTs during the calcination in air. For nano-$TiNb_2O_7$/CNTs calcined in N_2, however, its XRD peaks can conform to a $Ti_2Nb_{10}O_{29}$-type crystal structure ($Me_{12}O_{29}$-type monoclinic shear ReO_3 crystal structure with $A2/m$ space group constructed by $3 \times 4 \times \infty$ ReO_3-type blocks, JCPDS card No. 77-1374, Fig. 1b) with CNT impurities [33,34]. Previous studies confirmed that the calcinations of transition oxides in non-oxidizing atmospheres resulted in the generation of lower-valence cations and O^{2-} vacancies in crystal structures and thus the formation of nonstoichiometric oxides [29,35–37]. Therefore, the $TiNb_2O_7$ in nano-$TiNb_2O_7$/CNTs can be expressed as nonstoichiometric $Ti_4Nb_8O_{29-1-x}$ ($x > 0$) with some lower-valence cations (i.e., Ti^{3+} and Nb^{4+} ions) and a considerable amount of O^{2-} vacancies in the $Ti_2Nb_{10}O_{29}$-type structure.

Both nano-$TiNb_2O_7$ and nano-$TiNb_2O_7$/CNTs show broad XRD peaks, indicating their small grain sizes. Some peaks are so broad that they merge together. For instance, the two peaks marked by "^" in JCPDS card No. 77-1374 merge together to display a remarkably broad peak marked by "&" in nano-$TiNb_2O_7$/CNTs. Similarly, those marked by "*" correspond to only one broad marked by "@". The calcination temperature of nano-$TiNb_2O_7$ and nano-$TiNb_2O_7$/CNTs is only 700 °C, which is significantly lower than that of previous microsized $TiNb_2O_7$ particles from a traditional solid-state reaction method (1200 °C) [8]. Furthermore, during the calcination in N_2 (or

air), the existence of CNTs (or the production of CO_2 gas from the oxidation of CNTs) can effectively hinder the $TiNb_2O_7$ particle growth. Clearly, the low calcination temperature together with the addition of CNTs led to the small grain sizes and the broad XRD peaks in both samples. In comparison with nano-$TiNb_2O_7$, nano-$TiNb_2O_7$/CNTs shows broader XRD peaks, indicating its smaller grain sizes.

Fig. 3a and b present the FESEM images of the nano-$TiNb_2O_7$ sample. Its particle sizes vary from 20 to 200 nm. No nanotubes can be observed, verifying the complete combustion of CNTs during the calcination in air. In Fig. 3c and d, the FESEM images of the nano-$TiNb_2O_7$/CNTs composite reveal that the CNTs with an average diameter of ~50 nm were stochastically intercalated into the $TiNb_2O_7$ nanoparticles, which have smaller particle sizes than pure nano-$TiNb_2O_7$. During the fabrication process of nano-$TiNb_2O_7$/CNTs, its precursors were persistently stirred until the solvent was completely volatilized to ensure the uniform dispersion of the CNTs in the $TiNb_2O_7$ nanoparticles. Guaranteeing the precursor uniformity is the key to obtain the uniform nano-$TiNb_2O_7$/CNTs composite.

In order to further investigate the morphologies and microstructures of nano-$TiNb_2O_7$ and nano-$TiNb_2O_7$/CNTs, their TEM, HRTEM and selected-area electron diffraction pattern (SAED) images were recorded. As can be seen in Fig. 4a, the $TiNb_2O_7$ nanoparticles in the nano-$TiNb_2O_7$ sample combine with each other, forming an aggregation structure. Its HRTEM image in Fig. 4b shows lattice fringes with lattice spacings of 0.361 and 0.346 nm, which respectively correspond to ($\bar{1}11$) and (401) crystallographic planes of $TiNb_2O_7$ crystals. In contrast, the CNTs and $TiNb_2O_7$ nanoparticles have good contact and are well mixed in the nano-$TiNb_2O_7$/CNTs sample (Fig. 4c and d). Such a structure is beneficial for the electrical conduction among the $TiNb_2O_7$ nanoparticles. The clear lattice fringe with a lattice spacing of 0.338 nm matches well with (002) planes of CNTs (Fig. 4d). The one with 0.356 nm (Fig. 4e) perfectly matches with the (400) plane of the $Ti_2Nb_{10}O_{29}$-type structure and the (400) XRD peak at ~25° (Fig. 2). It should be mentioned that this spacing cannot match with any planes of the $TiNb_2O_7$ crystals since no peaks appear at ~25° in the XRD pattern of $TiNb_2O_7$. Furthermore, the sharp spots in the SAED image of the $TiNb_2O_7$ nanoparticle (Fig. 4f) perfectly correspond to ($\bar{1}10$), (511) and (601) planes of the $Ti_2Nb_{10}O_{29}$-type structure. These results further confirm the $Ti_2Nb_{10}O_{29}$-type structure of $TiNb_2O_7$ in the composite.

Fig. 5 shows the N_2 adsorption–desorption isotherms of nano-$TiNb_2O_7$ and nano-$TiNb_2O_7$/CNTs. As can be seen, each isotherm displays a distinct loop in the relative pressure range of 0.8–1.0. Thus, they can be classified as type IV of N_2 adsorption-desorption curves (IUPAC classification), indicating that both the samples are mesoporous materials [38–42]. The mesoporous characteristics are also demonstrated by their BJH desorption pore size distributions (the inset of Fig. 5). The average pore size of nano-$TiNb_2O_7$ (21.6 nm) is slightly larger than that of nano-$TiNb_2O_7$/CNTs (18.5 nm), probably due to the loss of CNTs during the calcination in air. However, nano-$TiNb_2O_7$/CNTs exhibits an obviously larger pore volume (0.110 cm^3 g^{-1}) than nano-$TiNb_2O_7$ (0.083 cm^3 g^{-1}), verifying the less severe particle aggregation in nano-$TiNb_2O_7$/CNTs. The BET specific surface areas of nano-$TiNb_2O_7$ and nano-$TiNb_2O_7$/CNTs are 12.9 and 18.1 m^2 g^{-1}, respectively. Since nano-$TiNb_2O_7$/CNTs contains 9.1 wt% CNTs with a specific surface area of 46.4 m^2 g^{-1} (Fig. S1), the specific surface area of the $TiNb_2O_7$ nanoparticles in the composite can be calculated to be 15.3 m^2 g^{-1}, which is larger than that of nano-$TiNb_2O_7$. This increase is in good agreement with the smaller $TiNb_2O_7$ particle sizes (Figs. 3d and 4c).
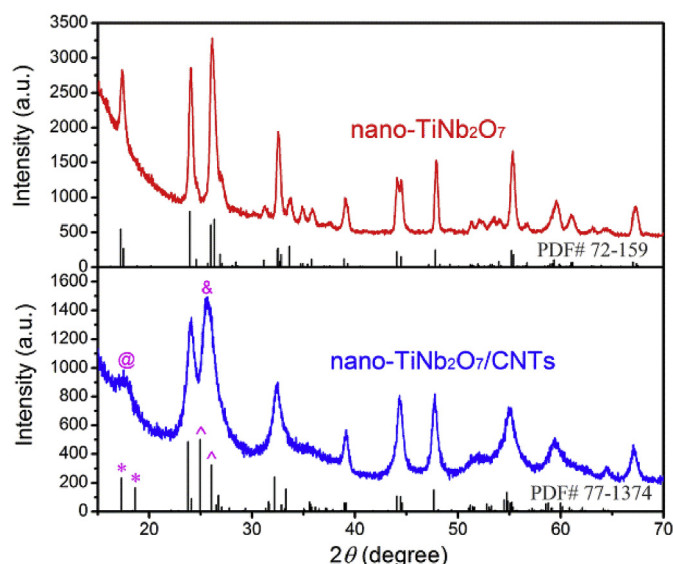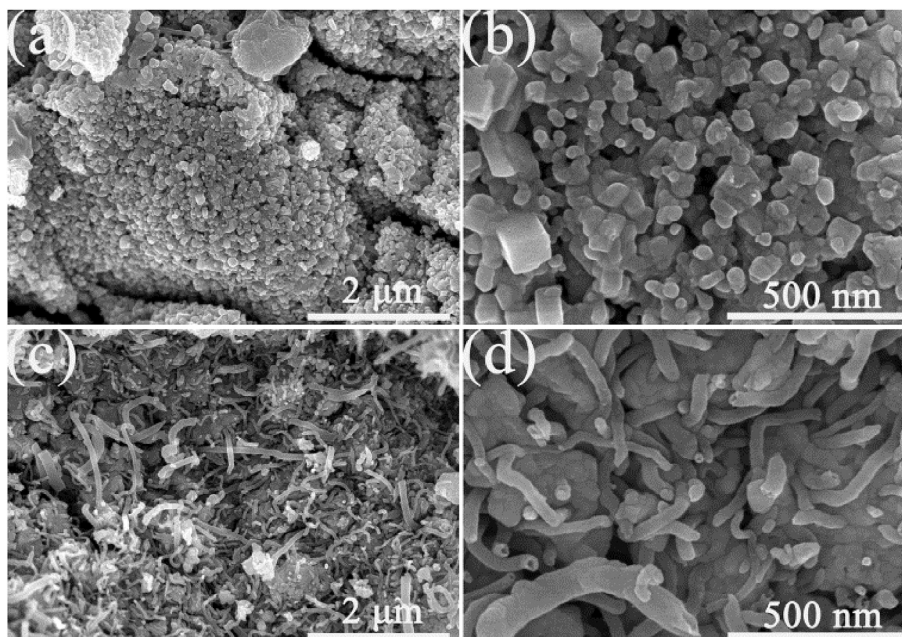

Fig. 2. XRD patterns of nano-$TiNb_2O_7$ and nano-$TiNb_2O_7$/CNTs.

Fig. 3. FESEM images of (a, b) nano-TiNb$_2$O$_7$ and (c, d) nano-TiNb$_2$O$_7$/CNTs.

3.2. Electrochemical performances

CV tests were implemented on the nano-TiNb$_2$O$_7$‖Li and nano-TiNb$_2$O$_7$/CNTs‖Li cells in a potential range of 3.0–0.8 V to clarify their electrochemical mechanisms. Fig. 6a, b and c record and compare their CV curves, in which the first four cycles were operated at 0.2 mV s^{-1} and the last three cycles at 0.4, 0.7 and 1.1 mV s^{-1}, respectively. As can be seen from Fig. 6a, the locations of the cathodic CV peaks shift to larger potentials after the first cycle, which could be due to the irreversible lithiation during the first cycle [43]. From the second cycle of the nano-TiNb$_2$O$_7$‖Li cell in Fig. 6a, a pair of intensive cathodic/anodic peaks centered at 1.60/1.73 V can be assigned to the redox reaction of Nb^{4+}/Nb^{5+} redox couple [44]. A pair of shoulder peaks at 1.89/2.03 V can be ascribed to the Ti^{3+}/Ti^{4+} redox couple. A pair of broad peaks at 1.01/1.31 V can be related to the Nb^{3+}/Nb^{4+} redox couple. For the nano-TiNb$_2$O$_7$/CNTs‖Li cell, besides the same three pairs of CV peaks at similar potentials, no other peaks can be observed. Thus, the presence of CNTs and the crystal-structure change of TiNb$_2$O$_7$ do not obviously affect the redox behavior of TiNb$_2$O$_7$ in 3.0–0.8 V. However, compared with the nano-TiNb$_2$O$_7$‖Li cell, the nano-TiNb$_2$O$_7$/CNTs‖Li cell shows larger peak intensities (Fig. 6a–c). Therefore, the nano-TiNb$_2$O$_7$/CNTs sample exhibits better electrochemical kinetics [45,46], which undoubtedly benefit the rate capability.

A linear relationship between the peak current density i_p of the intensive cathodic/anodic peaks at ~1.6/1.7 V and the square root of the scan speed $v^{0.5}$ can be found in Fig. 6d, which reveals the linear semi-infinite diffusion in the cathodic/anodic processes. Consequently, the apparent Li$^+$-ion diffusion coefficients D of nano-TiNb$_2$O$_7$ and nano-TiNb$_2$O$_7$/CNTs can be calculated through the Randles-Sevcik Equation (1) [47]:

$$i_p = 2.69 \times 10^5 \times n^{1.5} SCD^{0.5} v^{0.5} \qquad (1)$$

where n, S and C refer to the charge transfer number, the surface area of TiNb$_2$O$_7$ per unit weight, and the molar concentration of Li$^+$ ions in solid, respectively. The apparent Li$^+$-ion diffusion coefficients of nano-TiNb$_2$O$_7$ is 8.01×10^{-16} cm^2 s^{-1} (lithiation) and 9.52×10^{-16} cm^2 s^{-1} (delithiation), while those for nano-TiNb$_2$O$_7$/CNTs are larger, reaching 9.27×10^{-16} cm^2 s^{-1} (lithiation) and 1.37×10^{-15} cm^2 s^{-1} (delithiation). These improvements can be ascribed to the crystal structure modification of TiNb$_2$O$_7$ in nano-TiNb$_2$O$_7$/CNTs. The considerable amount of O^{2-} vacancies in the Ti$_2$Nb$_{10}$O$_{29}$-type TiNb$_2$O$_7$ can provide more Li$^+$-ion transport pathways in the crystals and thus facilitate the Li$^+$-ion transport [48,49].

The galvanostatic discharge–charge tests of the nano-TiNb$_2$O$_7$‖Li and nano-TiNb$_2$O$_7$/CNTs‖Li cells were executed at different current rates (1 C = 388 mA g^{-1}) within the potential range of 3.0–0.8 V, as shown in Fig. 7a. At all the current rates, the nano-TiNb$_2$O$_7$/CNTs sample always exhibits larger capacities than the nano-TiNb$_2$O$_7$ sample. At 0.1 C, the reversible capacity of the nano-TiNb$_2$O$_7$ sample is 344 mAh g^{-1}, while the nano-TiNb$_2$O$_7$/CNTs sample shows a slightly increased reversible capacity, i.e., 346 mAh g^{-1}. It is noteworthy that these practical capacities are approximately double that of the popular Li$_4$Ti$_5$O$_{12}$ (~170 mAh g^{-1}). With increasing the current rate, the capacity difference of these two samples is monotonically increased. When the nano-TiNb$_2$O$_7$ sample delivers a capacity of 183 mAh g^{-1} at 10 C, the nano-TiNb$_2$O$_7$/CNTs sample provides 40 mAh g^{-1} more, reaching 223 mAh g^{-1}. At 30 C (only 120 s to full discharge/charge), the nano-TiNb$_2$O$_7$/CNTs sample still offers a large capacity of 163 mAh g^{-1}, which is even ~1.7 times that of the nano-TiNb$_2$O$_7$ sample at 20 C (94 mAh g^{-1}). This superior rate capability of nano-TiNb$_2$O$_7$/CNTs is among the best results ever reported on the TiNb$_2$O$_7$ materials (Fig. 7b) [8–27], which can be due to the synergistic effects of four improvements. The Li$^+$-ion diffusion coefficient of nano-TiNb$_2$O$_7$/CNTs was improved due to the formation of O^{2-} vacancies. The production of the lower-valence cations with free d-band electrons in TiNb$_2$O$_7$ can improve its electronic conductivity. In addition, the presence of CNTs is capable of not only reducing the TiNb$_2$O$_7$ particle sizes but also improving the electrical conduction among the TiNb$_2$O$_7$ nanoparticles.

Fig. 7c displays the cyclic stability of the nano-TiNb$_2$O$_7$‖Li and nano-TiNb$_2$O$_7$/CNTs‖Li cells at 10 C. The nano-TiNb$_2$O$_7$/CNTs

Fig. 4. (a) TEM image of nano-TiNb$_2$O$_7$, (b) HRTEM image of a TiNb$_2$O$_7$ nanoparticle in nano-TiNb$_2$O$_7$, (c) TEM image of nano-TiNb$_2$O$_7$/CNTs, (d) HRTEM image of a CNT and a TiNb$_2$O$_7$ nanoparticle in nano-TiNb$_2$O$_7$/CNTs, (e) HRTEM image of a TiNb$_2$O$_7$ nanoparticle in nano-TiNb$_2$O$_7$/CNTs and (f) SAED image of a TiNb$_2$O$_7$ nanoparticle in nano-TiNb$_2$O$_7$/CNTs.

sample possesses outstanding cyclic stability with a largely retained capacity of 218 mAh g^{-1} after 100 cycles, corresponding to small capacity loss of only 2.4%. Meanwhile, its Coulombic efficiency was always maintained at ~100%. In contrast, the nano-TiNb$_2$O$_7$ sample shows relatively large capacity loss of 7.2% at the same current rate.

In order to further investigate the electrochemical performances of the nano-TiNb$_2$O$_7$‖Li and nano-TiNb$_2$O$_7$/CNTs‖Li cells, their EIS measurements were conducted and the resultant Nyquist plots are illustrated in Fig. 8. Each plot is composed of two depressed semicircles and one slope. According to a previous study [50], the

depressed semicircle in the high-frequency range can be ascribed to the synergistic effect of Li$^+$-ion adsorption, electron transfer and desolvation, which is denoted as R_1 and CPE$_1$ in the equivalent circuit (the inset of Fig. 8); the other depressed semicircle in the medium-frequency range can be attributed to the Li$^+$-ion insertion at particle surfaces (R_2 and CPE$_2$); and the slope in the low-frequency region can correspond to the Warburg resistance (W), reflecting the Li$^+$-ion diffusion within bulk crystals. R_b in the equivalent circuit represents the Ohmic resistance of the cell. The fitted R_1 and R_2 values for the nano-TiNb$_2$O$_7$ sample are 262 and 311 Ω, respectively. In sharp contrast, those for the nano-TiNb$_2$O$_7$/
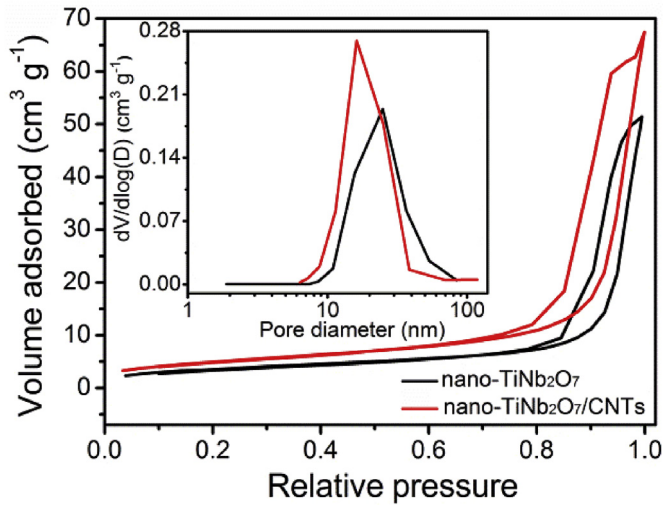
Fig. 5. N_2 adsorption−desorption isotherms of nano-TiNb$_2$O$_7$ and nano-TiNb$_2$O$_7$/CNTs. The inset shows their corresponding BJH desorption pore size distributions.

CNTs sample are significantly decreased to 109 and 129 Ω, indicating its significantly faster Li$^+$-ion adsorption, electron-transfer, desolvation and Li$^+$-ion insertion at particle surfaces. This improvement can be attributed to the better electronic/ionic conductivities of nano-TiNb$_2$O$_7$/CNTs and good contact between the CNTs and the TiNb$_2$O$_7$ nanoparticles. This EIS result is well

consistent with the better rate capability of the nano-TiNb$_2$O$_7$/CNTs‖Li cell (Fig. 7a and b).

4. Conclusions

Nano-TiNb$_2$O$_7$ with particle sizes of 20−200 nm was synthesized by direct hydrolysis followed by calcination in air. To further improve the electrochemical performances, novel nano-TiNb$_2$O$_7$/CNTs with 9.1 wt% CNTs was fabricated through the same method but calcined in N_2. Interestingly, the TiNb$_2$O$_7$ in the composite can be identified as nonstoichiometric Ti$_4$Nb$_8$O$_{29-1-x}$ ($x > 0$) with a Ti$_2$Nb$_{10}$O$_{29}$-type crystal structure, which contains lower-valence cations (Ti^{3+} and Nb^{4+} ions) and O^{2-} vacancies. The free $3d/4d$ electrons in the Ti^{3+}/Nb^{4+} ions can easily transport in the TiNb$_2$O$_7$ crystals, thereby increasing the electronic conductivity of TiNb$_2$O$_7$. The O^{2-} vacancies can facilitate the Li$^+$-ion transport, thereby improving the Li$^+$-ion diffusion coefficient of TiNb$_2$O$_7$. The good contact between the CNTs and the TiNb$_2$O$_7$ particles is capable of reducing the sizes of the TiNb$_2$O$_7$ particles and enhancing the electrical conduction among them. Consequently, nano-TiNb$_2$O$_7$/CNTs exhibits a significantly better rate capability than nano-TiNb$_2$O$_7$. At 0.1 C, nano-TiNb$_2$O$_7$/CNTs delivers a large capacity of 346 mAh g^{-1}, similar to that of nano-TiNb$_2$O$_7$ (344 mAh g^{-1}). At 30 C, however, the capacity of nano-TiNb$_2$O$_7$/CNTs still reaches 163 mAh g^{-1}, significantly larger than that of nano-TiNb$_2$O$_7$ at 20 C (94 mAh g^{-1}). Furthermore, nano-TiNb$_2$O$_7$/CNTs presents superior cyclic stability as demonstrated in over 100 cycles at 10 C with a small capacity loss of only 2.4%, in contrast to the value of 7.2% for nano-TiNb$_2$O$_7$. Clearly, nano-TiNb$_2$O$_7$/CNTs fulfills the four
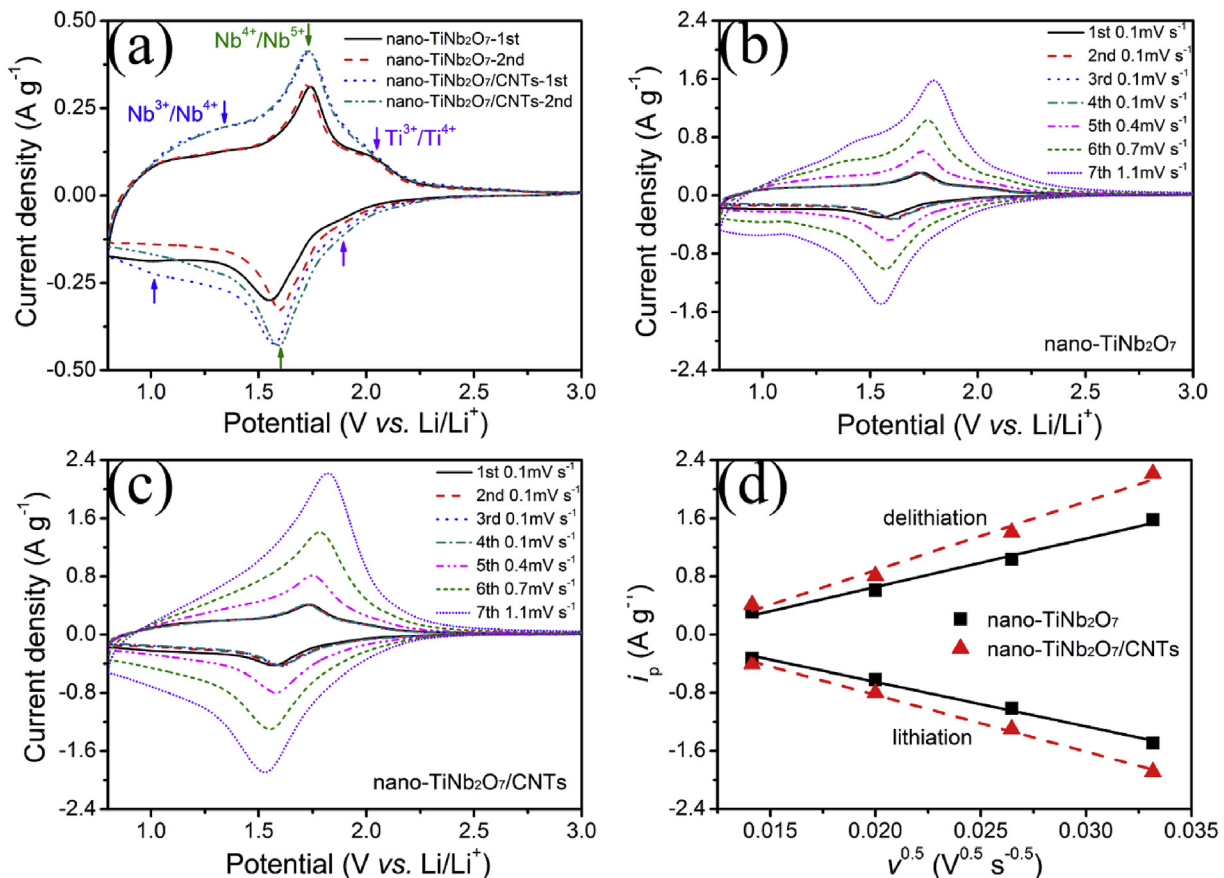

Fig. 6. CV curves of nano-TiNb$_2$O$_7$‖Li and nano-TiNb$_2$O$_7$/CNTs‖Li cells at (a) 0.2 mV s^{-1} and (b, c) various scan speeds. (d) Relationship between peak current density of cathodic/anodic reaction i_p and square root of scan speed $v^{0.5}$.
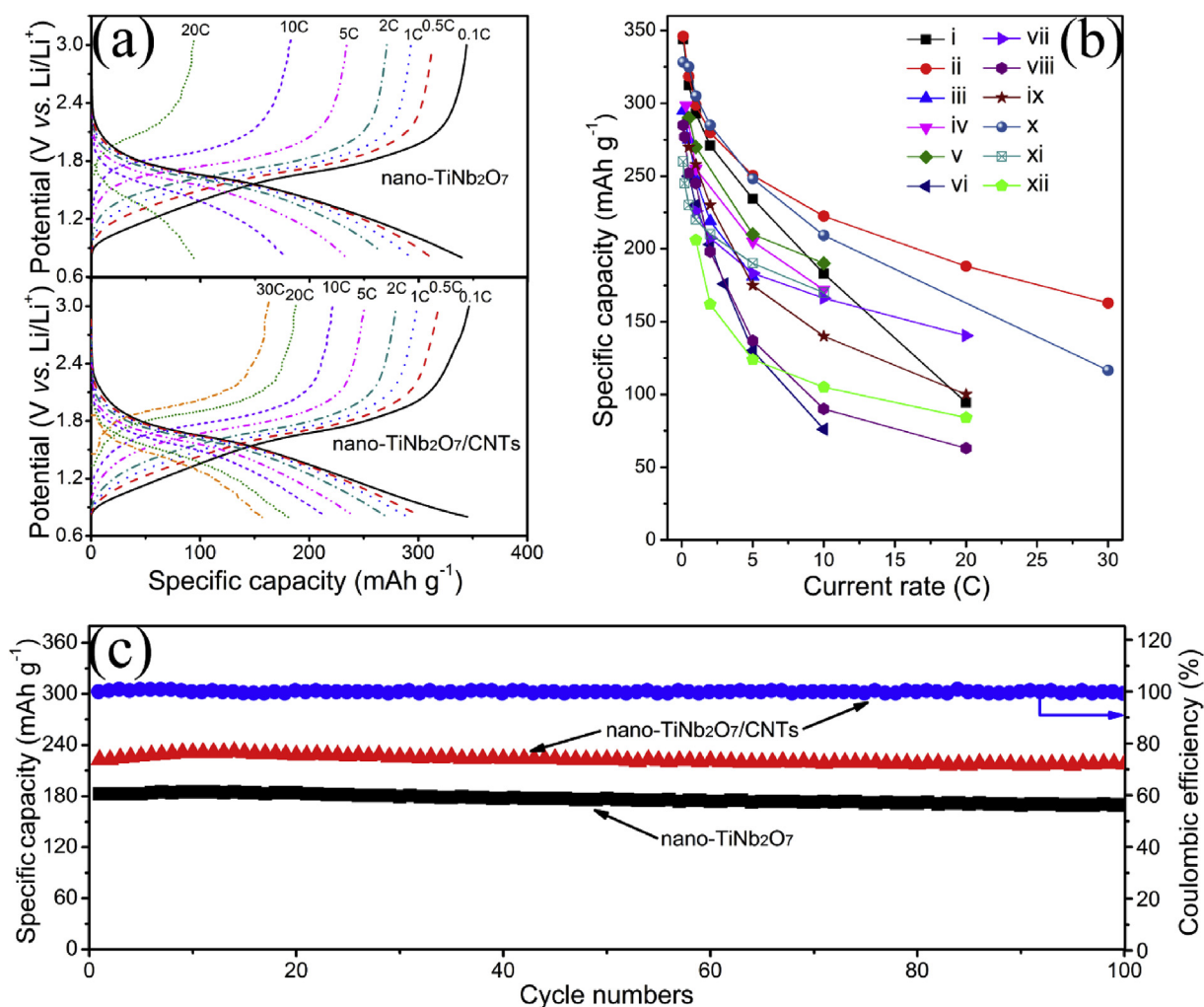
Fig. 7. Electrochemical performances of nano-TiNb$_2$O$_7$‖Li and nano-TiNb$_2$O$_7$/CNTs‖Li cells: (a) discharge–charge curves at 0.1–30 C; (b) comparison of rate capabilities of nano-TiNb$_2$O$_7$ and nano-TiNb$_2$O$_7$/CNTs with previously reported TiNb$_2$O$_7$ materials: (i) nano-TiNb$_2$O$_7$ (this work), (ii) nano-TiNb$_2$O$_7$/CNTs (this work), (iii) Ru$_{0.01}$Ti$_{0.99}$Nb$_2$O$_7$ microsized particles (Ref. [8]), (iv) V$_{0.02}$TiNb$_{1.98}$O$_7$ microsized particles (Ref. [16]), (v) Mo$_{0.05}$Ti$_{0.95}$Nb$_2$O$_7$ nanoparticles (Ref. [19]), (vi) TiNb$_2$O$_7$ nanoparticles (Ref. [23]), (vii) TiNb$_2$O$_7$ nanorods (Ref. [10]), (viii) TiNb$_2$O$_7$ nanofibers (Ref. [22]), (ix) TiNb$_2$O$_7$ mesoporous microspheres (Ref. [11]), (x) TiNb$_2$O$_7$ ordered nanotubes (Ref. [15]), (xi) TiNb$_2$O$_7$/graphene nanocomposite (Ref. [18]) and (xii) TiNb$_2$O$_7$ ordered macroporous particles (Ref. [24]); and (c) cyclic stability at 10 C. Identical discharge–charge rates were used.
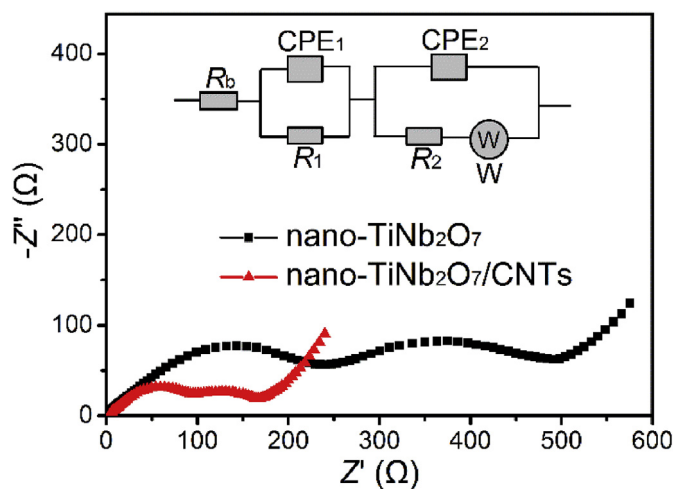

Fig. 8. Nyquist plots of nano-TiNb$_2$O$_7$‖Li and nano-TiNb$_2$O$_7$/CNTs‖Li cells. The inset exhibits the equivalent circuit to fit the plots, in which R, CPE and W represent resistance, constant phase element and Warburg resistance, respectively.

requirements of high energy density, power density, safety and cyclic stability, and thus has potential applications in high-performance LIBs of EVs.

Appendix A. Supplementary data

Supplementary data related to this article can be found at https://doi.org/10.1016/j.electacta.2017.11.051.

References

[1] M. Armand, J.M. Tarascon, Building better batteries, Nature 451 (2008) 652–657.
[2] S.S. Zheng, The effect of the charging protocol on the cycle life of a Li-ion battery, J. Power Sources 161 (2006) 1385–1391.
[3] S.M. Aqeel, Z.Y. Huang, J. Walton, C. Baker, D. Falkner, Z. Liu, Z. Wang,

Polyvinylidene fluoride (PVDF)/polyacrylonitrile (PAN)/carbon nanotube nanocomposites for energy storage and conversion, Adv. Compos. Hybrid. Mater. (2017). https://doi.org/10.1007/s42114-017-0002-5.

[4] C. Cheng, R. Fan, Z. Wang, Q. Shao, X. Guo, P. Xie, Y. Yin, Y. Zhang, L. An, Y. Lei, J. Ryu, A. Shankar, Z. Guo, Tunable and weakly negative permittivity in carbon/silicon nitride composites with different carbonizing temperatures, Carbon 125 (2017) 103−112.

[5] C.F. Lin, C. Yang, S.W. Lin, J.B. Li, Titanium-containing complex oxides as anode materials for lithium-ion batteries: a review, Mater. Technol. 30 (2015) 192−202.

[6] J.T. Han, Y.H. Huang, J.B. Goodenough, New anode framework for rechargeable lithium batteries, Chem. Mater. 23 (2011) 2027−2029.

[7] C. Yang, C.F. Lin, S.W. Lin, Y.J. Chen, J.B. Li, $Cu_{0.02}Ti_{0.94}Nb_{2.04}O_7$: an advanced anode material for lithium-ion batteries of electric vehicles, J. Power Sources 328 (2016) 336−344.

[8] C.F. Lin, S. Yu, S.Q. Wu, S.W. Lin, Z.Z. Zhu, J.B. Li, L. Lu, $Ru_{0.01}Ti_{0.99}Nb_2O_7$ as an intercalation-type anode material with a large capacity and high rate performance for lithium-ion batteries, J. Mater. Chem. A 3 (2015) 8627−8635.

[9] L. Buannic, J.F. Colin, M. Chapuis, M. Chakir, S. Patoux, Electrochemical performances and gassing behavior of high surface area titanium niobium oxides, J. Mater. Chem. A 4 (2016) 11531−11541.

[10] S.F. Lou, Y.L. Ma, X.Q. Cheng, J.L. Gao, Y.Z. Gao, P.J. Zuo, C.Y. Du, G.P. Yin, Facile synthesis of nanostructured $TiNb_2O_7$ anode materials with superior performance for high-rate lithium ion batteries, Chem. Commun. 51 (2015) 17293−17296.

[11] H.S. Li, L.F. Shen, G. Pang, S. Fang, H.F. Luo, K. Yang, X.G. Zhang, $TiNb_2O_7$ nanoparticles assembled into hierarchical microspheres as high-rate capability and long-cycle-life anode materials for lithium ion batteries, Nanoscale 7 (2015) 619−624.

[12] H. Park, H.B. Wu, T. Song, X.W. Lou, U. Paik, Porosity-controlled $TiNb_2O_7$ microspheres with partial nitridation as a practical negative electrode for high-power lithium-ion batteries, Adv. Energy Mater. 5 (2015), 1401945.

[13] H. Park, T. Song, U. Paik, Porous $TiNb_2O_7$ nanofibers decorated with conductive $Ti_{1−x}Nb_xN$ bumps as a high power anode material for Li-ion batteries, J. Mater. Chem. A 3 (2015) 8590−8596.

[14] Q.S. Cheng, J.W. Liang, N. Lin, C. Guo, Y.C. Zhu, Y.T. Qian, Porous $TiNb_2O_7$ nanospheres as ultra long-life and high-power anodes for lithium-ion batteries, Electrochim. Acta 176 (2015) 456−462.

[15] H.S. Li, L.F. Shen, J. Wang, S. Fang, Y.X. Zhang, H. Dou, X.G. Zhang, Three-dimensionally ordered porous $TiNb_2O_7$ nanotubes a superior anode material for next generation hybrid supercapacitors, J. Mater. Chem. A 3 (2015) 16785−16790.

[16] X.Y. Wen, C.X. Ma, C.Q. Du, J. Liu, X.H. Zhang, D.Y. Qu, Z.Y. Tang, Enhanced electrochemical properties of vanadium-doped titanium niobate as a new anode material for lithium-ion batteries, Electrochim. Acta 186 (2015) 58−63.

[17] S. Li, X. Cao, C.N. Schmidt, Q. Xu, E. Uchaker, Y. Pei, G.Z. Cao, $TiNb_2O_7$/graphene composites as high-rate anode materials for lithium/sodium ion batteries, J. Mater. Chem. A 4 (2016) 4242−4251.

[18] A.G. Ashish, P. Arunkumar, B. Babu, P. Manikandan, S. Sarang, M.M. Shaijumon, $TiNb_2O_7$/graphene hybrid material as high performance anode for lithium-ion batteries, Electrochim. Acta 175 (2015) 285−292.

[19] H. Song, Y. Kim, A Mo-doped $TiNb_2O_7$ anode for lithium-ion batteries with high rate capability due to charge redistribution, Chem. Commun. 51 (2015) 9849−9852.

[20] C. Jo, Y. Kim, J. Hwang, J. Shim, J. Chun, J. Lee, Block copolymer directed ordered mesostructured $TiNb_2O_7$ multimetallic oxide constructed of nanocrystals as high power Li-ion battery anodes, Chem. Mater. 26 (2014) 3508−3514.

[21] B.K. Guo, X.Q. Yu, X.G. Sun, M.F. Chi, Z.A. Qiao, J. Liu, Y.S. Hu, X.Q. Yang, J.B. Goodenough, S. Dai, A long-life lithium-ion battery with highly porous $TiNb_2O_7$ anode for large-scale electrical energy storage, Energy Environ. Sci. 7 (2014) 2220−2226.

[22] K. Tang, X.K. Mu, P.A. van Aken, Y. Yu, J. Maier, "Nano-pearl-string" $TiNb_2O_7$ as anodes for rechargeable lithium batteries, Adv. Energy Mater 3 (2013) 49−53.

[23] L. Fei, Y. Xu, X.F. Wu, Y.L. Li, P. Xie, S.G. Deng, S. Smirnov, H.M. Luo, SBA-15 confined synthesis of $TiNb_2O_7$ nanoparticles for lithium-ion batteries, Nanoscale 5 (2013) 11102−11107.

[24] S.F. Lou, X.Q. Cheng, Y. Zhao, A. Lushington, J.L. Gao, Q. Li, P.J. Zuo, B.Q. Wang, Y.Z. Gao, Y.L. Ma, C.Y. Du, G.P. Yin, X.L. Sun, Superior performance of ordered macroporous $TiNb_2O_7$ anodes for lithium ion batteries: understanding from the structural and pseudocapacitive insights on achieving high rate capability, Nano Energy 34 (2017) 15−25.

[25] H. Park, D.H. Shin, T. Song, W.I. Park, J. Paik, Synthesis of hierarchical porous $TiNb_2O_7$ nanotubes with controllable porosity and their application in high power Li-ion batteries, J. Mater. Chem. A 5 (2017) 6958−6965.

[26] G.Y. Liu, X.D. Liu, Y.Y. Zhao, X.G. Ji, J.L. Guo, Synthesis of Ag-coated $TiNb_2O_7$ composites with excellent electrochemical properties for lithium-ion battery, Mater. Lett. 197 (2017) 38−40.

[27] H.X. Yu, H. Lan, L. Yan, S.S. Qian, X. Cheng, H.J. Zhu, N.B. Long, M. Shui, J. Shu,

[28] $TiNb_2O_7$ hollow nanofiber anode with superior electrochemical performance in rechargeable lithium ion batteries, Nano Energy 38 (2017) 109−117.

[28] C.F. Lin, X.Y. Fan, Y.L. Xin, F.Q. Cheng, M.O. Lai, H.H. Zhou, L. Lu, $Li_4Ti_5O_{12}$-based anode materials with low working potentials, high rate capabilities and high cyclability for high-power lithium-ion batteries: a synergistic effect of doping, incorporating a conductive phase and reducing particle size, J. Mater. Chem. A 2 (2014) 9982−9993.

[29] C.F. Lin, M.O. Lai, L. Lu, H.H. Zhou, Mesoporous $Li_4Ti_5O_{12−x}$/C submicrospheres with comprehensively improved electrochemical performances for high-power lithium-ion batteries, Phys. Chem. Chem. Phys. 16 (2014) 24874−24883.

[30] K.J. Ziegler, Z.N. Gu, H.Q. Peng, E.L. Flor, R.H. Hauge, R.E. Smalley, Controlled oxidative cutting of single-walled carbon nanotubes, J. Am. Chem. Soc. 127 (2005) 1541−1547.

[31] A. Kuznetsova, I. Popova, J.T. Yates, M.J. Bronikowski, C.B. Huffman, J. Liu, R.E. Smalley, H.H. Hwu, J.G. Chen, Oxygen-containing functional groups on single-wall carbon nanotubes: NEXAFS and vibrational spectroscopic studies, J. Am. Chem. Soc. 123 (2001) 10699−10704.

[32] A. Rochefort, P. Avouris, Electron interference effects on the conductance of doped carbon nanotubes, J. Phys. Chem. A 104 (2000) 9807−9810.

[33] X.Y. Wu, J. Miao, W.Z. Han, Y.S. Hu, D.F. Chen, J. Lee, J. Kim, L.Q. Chen, Investigation on $Ti_2Nb_{10}O_{29}$ anode material for lithium-ion batteries, Electrochem. Commun. 25 (2012) 39−42.

[34] X. Lou, C. Lin, Q. Luo, J. Zhao, B. Wang, J. Li, Q. Shao, X. Guo, N. Wang, Z. Guo, Crystal-structure modification enhanced $FeNb_{11}O_{29}$ anodes for lithium-ion batteries, ChemElectroChem (2017). https://doi.org/10.1002/celc.201700816.

[35] X.M. Chen, X.F. Guan, L.P. Li, G.S. Li, Defective mesoporous $Li_4Ti_5O_{12−y}$: an advanced anode material with anomalous capacity and cycling stability at a high rate of 20 C, J. Power Sources 210 (2012) 297−302.

[36] T. Liu, K. Yu, L. Gao, H. Chen, N. Wang, L. Hao, T. Li, H. He, Z. Guo, Graphene quantum dots decorated $SrRuO_3$ mesoporous film as an efficient counter electrode for high-performance dye-sensitized solar cells, J. Mater. Chem. A 5 (2017) 17848−17855.

[37] B. Song, T. Wang, H. Sun, Q. Shao, J. Zhao, K. Song, L. Hao, L. Wang, Z. Guo, Two-step hydrothermally synthesized carbon nanodots/WO_3 photocatalysts with enhanced photocatalytic performance, Dalton Trans. (2017). https://doi.org/10.1039/C7DT03003G.

[38] C.F. Lin, X.Y. Fan, Y.L. Yin, F.Q. Cheng, M.O. Lai, H.H. Zhou, L. Lu, Monodispersed mesoporous $Li_4Ti_5O_{12}$ submicrospheres as anode materials for lithium-ion batteries: morphology and electrochemical performances, Nanoscale 6 (2014) 6651−6660.

[39] Z.Y. Sun, L. Zhang, F. Dang, Y. Liu, Z.Y. Fei, Q. Shao, H. Lin, J. Guo, L.C. Xiang, N. Yerra, Z.H. Guo, Experimental and simulation-based understanding of morphology controlled barium titanate nanoparticles under co-adsorption of surfactants, CrystEngComm 19 (2017) 3288−3298.

[40] Y. Ma, L. Lyu, Y. Guo, Y. Fu, Q. Shao, T. Wu, S. Guo, K. Sun, X. Guo, E.K. Wujcik, Z. Guo, Porous lignin based poly (acrylic acid)/organo-montmorillonite nanocomposites: swelling behaviors and rapid removal of Pb (II) ions, Polymer 128 (2017) 12−23.

[41] C. Wang, Y. Wu, Y. Li, Q. Shao, X. Yan, C. Han, Z. Wang, Z. Liu, Z. Guo, Flame retardant rigid polyurethane foam with a phosphorus-nitrogen single intumescent flame retardant, Polym. Adv. Technol. (2017). https://doi.org/10.1002/pat.4105.

[42] Y.F. Tang, L. Yang, Z. Qiu, J.S. Huang, Template-free synthesis of mesoporous spinel lithium titanate microspheres and their application in high-rate lithium ion batteries, J. Mater. Chem. 19 (2009) 5980−5984.

[43] X. Lu, Z.L. Jian, Z. Fang, L. Gu, Y.S. Hu, W. Chen, Z.X. Wang, L.Q. Chen, Atomic-scale investigation on lithium storage mechanism in $TiNb_2O_7$, Energy Environ. Sci. 4 (2011) 2638−2644.

[44] X.F. Wang, G.Z. Shen, Intercalation pseudo-capacitive $TiNb_2O_7$@carbon electrode for high-performance lithium ion hybrid electrochemical supercapacitors with ultrahigh energy density, Nano Energy 15 (2015) 104−115.

[45] C.P. Han, Y.B. He, B.H. Li, H.F. Li, J. Ma, H.D. Du, X.Y. Qin, Q.H. Yang, F.Y. Kang, Highly crystalline lithium titanium oxide sheets coated with nitrogen-doped carbon enable high-rate lithium-ion batteries, ChemSusChem 7 (2014) 2567−2574.

[46] H. Noh, W. Choi, Preparation of a $TiNb_2O_7$ microsphere using formic acid and wrapping with reduced graphene oxide for anodes in lithium ion batteries, J. Electrochem. Soc. 163 (2016) A1042−A1049.

[47] A.J. Bard, L.R. Faulkner, Electrochemical Methods: Fundamentals and Applications, second ed., Wiley, New York, 2001.

[48] C.F. Lin, S. Yu, H. Zhao, S.Q. Wu, G.Z. Wang, L. Yu, Y.F. Li, Z.Z. Zhu, J.B. Li, S.W. Lin, Defective $Ti_2Nb_{10}O_{27.1}$: an advanced anode material for lithium-ion batteries, Sci. Rep. 5 (2015) 17836.

[49] C.F. Lin, G.Z. Wang, S.W. Lin, J.B. Li, L. Lu, $TiNb_6O_{17}$: a new electrode material for lithium-ion batteries, Chem. Commun. 51 (2015) 8970−8973.

[50] M. Nakayama, H. Ikuta, Y. Uchimoto, M. Wakihara, Study on the AC impedance spectroscopy for the Li insertion reaction of $Li_xLa_{1/3}NbO_3$ at the electrode-electrolyte interface, J. Phys. Chem. B 107 (2003) 10603−10607.